

## RESEARCH ARTICLE

View Article Online

View Journal | View Issue

Cite this: *Org. Chem. Front.*, 2024, **11**, 5741

## Conformationally enforced planarization of bis[1]benzothieno[1,4]thiazines: a rational design of redox-active fluorophores with increased radical cation stability†‡

Simone T. Hauer,<sup>a</sup> Patrick Kuhn,<sup>a</sup> J. Maurice Pütz,<sup>b</sup> Guido J. Reiss,<sup>b</sup> Lukas P. Sorge,<sup>c</sup> Christian Ganter,<sup>id</sup> Katja Heinze,<sup>id</sup> and Thomas J. J. Müller<sup>id</sup>\*<sup>a</sup>

A DFT-based approach guides the rational design of the substance class of *anti-anti*-bis[1]benzothieno[1,4]thiazines (BBTTs) bearing *N*-aryl substituents, previously generated as enhanced phenothiazine congeners, based upon the assumption that a minimization of the intrinsic butterfly folding in favor of a more planarized BBTT structure allows for better electronic tuning. Therefore, an intramolecular conformational restriction imposed by a sterically demanding *ortho*-(*ortho'*)-substitution pattern on *N*-aryl moieties is envisioned to provide this planarization of the BBTT's backbone, in solution and in the crystal solid state. Calculations of BBTT's minimum structures with variable *N*-aryl substitution as well as relaxed geometry PES scans assessing the energy barriers of the intramolecular restriction were carried out, identifying *anti-anti-N-ortho,ortho'*-disubstituted-phenyl-BBTTs as promising target structures. Synthetically, cyclizing Buchwald–Hartwig aminations starting from brominated sulfanes followed by subsequent functionalizations through organometallic catalysis and reagents pave the way to a substance library of the proposed BBTTs. Extensive structural analysis via X-ray diffraction reveals the molecular structures as well as the superordinate crystal packing patterns. NICS (nucleus-independent chemical shift) calculations indicate that strongly planarized BBTTs reveal a paratropic ring current and, therefore, an anti-aromatic character of their central 1,4-thiazine core. Comprehensive investigations of their optoelectronic properties by cyclic voltammetry, spectroelectrochemistry, and UV/vis absorption and emission spectroscopy shed light on the electronic structure, supported by aid of (TD)-DFT calculations. A broader range of their first redox potentials  $E_0^{0/+1}$ , larger semiquinone formation constants in comparison to *para-N*-aryl substituted BBTTs causing an increased radical cation stability, and a distinct tunability of their luminescence characteristics render *ortho*-(*ortho'*)-substituted BBTTs as highly functional strong donor moieties for future application in various fields.

Received 23rd June 2024,  
Accepted 22nd August 2024

DOI: 10.1039/d4qo01155d

rsc.li/frontiers-organic

## Introduction

Organic electronics are commercially and technologically gaining dominance, for instance by the implementation of organic light emitting diodes (OLEDs), organic field effect transistors (OFETs), or organic photovoltaics (OPVs).<sup>1</sup> Their functional principle is based on organic semiconductors (OSCs) as active parts, characterized by the electronic properties of their expanded  $\pi$ -conjugated systems.<sup>2</sup> This mainly relies on the molecule's electronic structure, which is often fine-tunable by rational design whereby the desired properties can be achieved.<sup>2a</sup> In this spirit, we aim to further refine the substance class of bis[1]benzothieno[1,4]thiazines (BBTT) (Fig. 1).

BBTTs were previously conceptualized as enhanced phenothiazine (PTZ) congeners by a formal double thieno expansion.<sup>3</sup> Especially BBTTs' *anti-anti*-regioisomers reveal fine-tunable, sig-

<sup>a</sup>Institut für Organische Chemie und Makromolekulare Chemie, Heinrich-Heine-Universität Düsseldorf, Universitätsstraße 1, D-40225 Düsseldorf, Germany.

E-mail: Thomas.J.Mueller@hhu.de

<sup>b</sup>Institut für Anorganische Chemie und Strukturchemie, Heinrich-Heine-Universität Düsseldorf, Universitätsstraße 1, D-40225 Düsseldorf, Germany<sup>c</sup>Institut für Chemie, Johannes-Gutenberg-Universität Mainz, Duesbergweg 10-14, D-55128 Mainz, Germany

†Dedicated to Prof. Dr. Frank Würthner on the occasion of his 60th birthday.

‡Electronic supplementary information (ESI) available. CCDC 2346002, 2345988, 2345990, 2345982, 2345989, 2345999, 2345994, 2345996, 2335542, 2335553, 2345957, 2345956, 2345983, 2345987, 2345959, 2345998, 2345948, 2345958, 2345985, 2345992, 2345944, 2346000 and 2345986. For ESI and crystallographic data in CIF or other electronic format see DOI: <https://doi.org/10.1039/d4qo01155d>

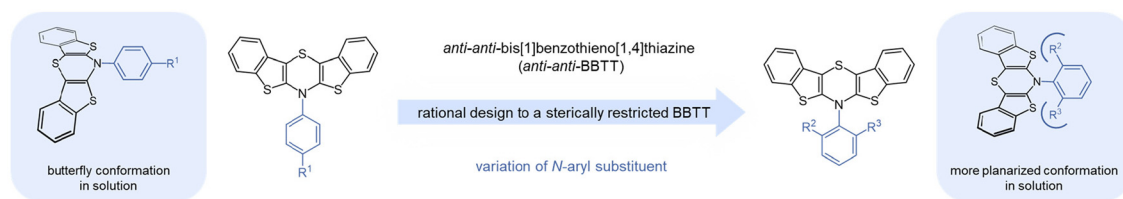


Fig. 1 Concept of the rational design of *anti-anti*-BBTTs to enforced conformational planarization through variation of the *N*-aryl substituent.

nificantly lowered first oxidation potentials with a high radical cation stability and intense emission.<sup>4</sup> For overcoming the inherent  $4n-\pi$ -antiaromaticity of the central 1,4-thiazine, conjugated BBTTs generally, like their PTZ congeners, adopt a butterfly-like structure. Folding along the *S,N*-axis of the 1,4-thiazine core places *N*-substituents either in an *N-intra* (pseudo equatorial) or *N-extra* (pseudo axial) conformation.

Therefore, it is particularly impressive that *anti-anti*-BBTTs are outstandingly the first anellated 1,4-thiazines exhibiting antiaromatic character due to planarization in the crystalline solid state.<sup>4a,c</sup> Subsequently, BBTTs as strong donors can be seen as enhanced substitutes for PTZ as an interesting potential OSC. Here, we present the rational design of enforced conformationally enhanced planarization of BBTTs by the *N*-aryl substituent, from computation over synthesis of a compound library and structural characterization in the solid state to electronic properties in the electronic ground and excited states.

## Results and discussion

### DFT-supported rational design

For enhancing the planarization in solution, as observed in the crystalline solid state, folding of the butterfly structure needs to be suppressed. This enforced planarization should promote  $\pi$ - $\pi$ -stacking and enhance the antiaromatic character of BBTTs even in solution. Hence, the rational design commences with controlling BBTT's conformation as the promising variable. A DFT-based approach is taken aspiring an underlying intramolecular restriction of BBTT's scaffold. Since all known BBTTs planarized in the crystalline solid state bear an *N*-phenyl moiety, often substituted in the *para*-position, those were chosen as a starting point. From here on, a computational screen for minimum geometries by varying the *N*-aryl moiety with different methyl decorations is launched (Fig. 2). A modified constitution by an *ortho,ortho'*-decoration of the *N*-aryl results in a pronounced sterically restricted BBTT's backbone inducing an increase in planarization (B3LYP/6-311++G\*\*, IEFCPCM CH<sub>2</sub>Cl<sub>2</sub>).<sup>5</sup> All postulated geometries reveal BBTTs adopting an *N-intra* conformation, thus the *N*-aryl substituents are orthogonally twisted with respect to the BBTTs' scaffolds. The concept is further supported by employing a relaxed geometry potential energy surface scan (PES scan) of *N*-aryls torsion exemplarily for *anti-anti-N-ortho,ortho'*-dimethylphenyl-BBTT **3i** (Fig. 3).

This forces a conformational change from the *N-intra* conformer (minimum geometry) to the *N-extra* conformer (B3LYP/

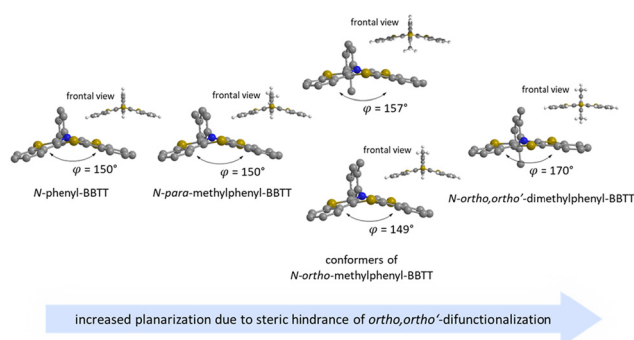


Fig. 2 Visualization of sterically restricted BBTTs due to the introduction of sterically demanding *ortho,ortho'*-substitution pattern (B3LYP/6-311++G\*\*, IEFCPCM CH<sub>2</sub>Cl<sub>2</sub>).

6-311G\*\*, IEFCPCM CH<sub>2</sub>Cl<sub>2</sub>). The resulting *N-extra* conformer does not appear as a second local minimum, but rather as a transition state between both *N-intra* conformers. The energy barrier in SCF energy as well as the difference in Gibbs free energy amount to 24.0 and 28.3 kcal mol<sup>-1</sup>, indicating a free rotation at room temperature to be unlikely. Therefore, the significantly more folded *N-extra* conformation should be suppressed. Determination of the equilibrium constant  $K_{\text{intra} \rightarrow \text{extra}}$  to  $1.90 \times 10^{-21}$  via Gibbs free energy difference quantifies this, resulting in a Boltzmann distribution of *N-intra* and *N-extra* conformer of 100 : 0 at 298 K. Furthermore, a change of conformation could also occur by ring inversion via a planar transition state. This can also be approximated by a relaxed geometry PES scan (B3LYP/6-311G\*\*, IEFCPCM CH<sub>2</sub>Cl<sub>2</sub>). Contrary to expectations no conformational change between *N-intra* and *N-extra* conformer arises. Instead an *N-intra-intra* equilibration occurs, which is particularly interesting for a heterogenic *ortho,ortho'*-substitution pattern. Significantly lower energy barriers in SCF energy and Gibbs free energy of <1 and 1.63 kcal mol<sup>-1</sup> indicate a free ring inversion at 298 K to be anticipated. The ratio of the *N-intra* conformer to the respective transition state can be determined to 94 : 6 via the equilibrium constant  $K_{\text{intrats}}$  of  $6.37 \times 10^{-2}$ .

### Modular synthesis

Synthesis follows up on our reliable established route to anellated 1,4-thiazines such as dithieno[1,4]thiazines (DTTs) and BBTTs via Buchwald-Hartwig amination.<sup>3,4b,6</sup> This previous concept has been adapted for the synthesis of sterically



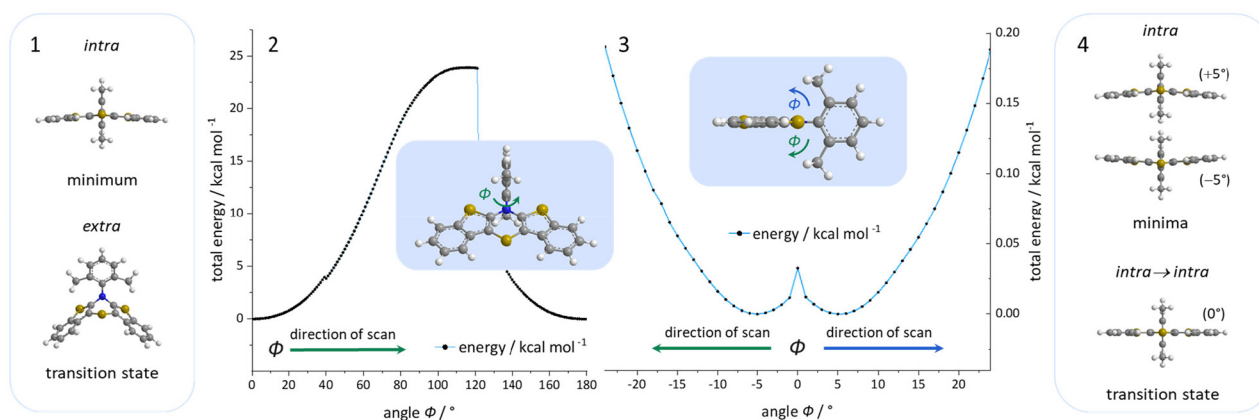
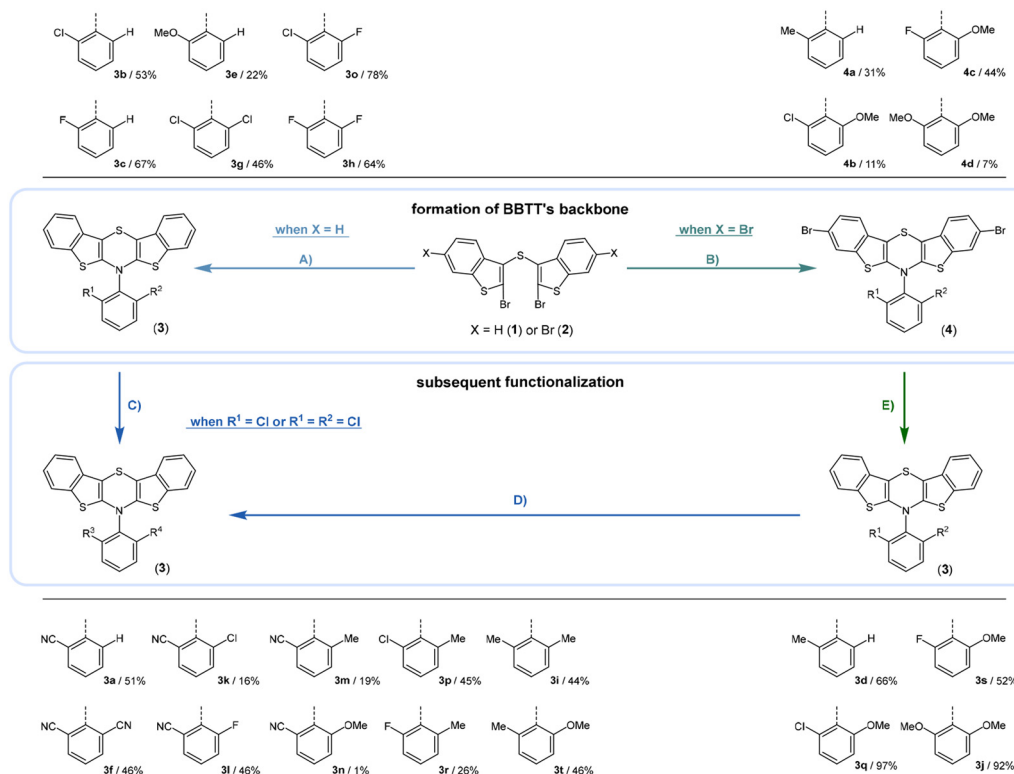


**Fig. 3** Visualization of the relaxed geometry PES scans of *N*-inversion (2) and ring inversion (3) of *N*-aryls by the angle  $\phi$  of **3i** (B3LYP/6-311G\*\*, IEPCPC  $\text{CH}_2\text{Cl}_2$ ). Most relevant minimum and transition state geometries of the relaxed geometry PES scan of *N*-inversion (1) and ring inversion (4) (B3LYP/6-311G\*\*, IEPCPC  $\text{CH}_2\text{Cl}_2$ ).

restricted *anti-anti*-BBTs **3** using the dibrominated sulfane **1** and, in this case, respective *ortho*(*ortho'*)-disubstituted anilines (Scheme 1). Whilst the previously employed ligand DPPF was only successfully applicable for *ortho*-substituted anilines,<sup>4b</sup> for *ortho,ortho'*-disubstituted anilines the adaption with

XantPhos as a ligand results in a breakthrough to satisfactory yields. Upon the sterically more demanding *ortho*(*ortho'*)-substitution pattern efficiency of the coupling still overall dropped in favor of the intramolecular reductive *C*-*C*-coupling of the starting material, resulting in dibenzo[*d,d'*]thieno[3,2-*b'*;4,5-*b'*]



**Scheme 1** Modular synthesis of sterically restricted BBTs **3** yielding a functionalization with electron accepting to electron donating substituents in the *ortho* or *ortho,ortho'*-position of the *N*-aryl moiety: (A) *ortho*(*ortho'*)-disubstituted aniline (1.00 equiv.),  $\text{Pd}(\text{dba})_2$  (5.00–7.50 mol%), DPPF or XantPhos (10.0–15.0 mol%),  $\text{NaO}^t\text{Bu}$  (3.00 equiv.), 110 °C in toluene; (B) *ortho*(*ortho'*)-aniline (1.00 equiv.),  $\text{Pd}(\text{dba})_2$  (3.00–5.00 mol%), BINAP (5.00–10.0 mol%),  $\text{NaO}^t\text{Bu}$  (3.00 equiv.), 110 °C in toluene; (C)  $\text{MeMgCl}$  (1.20–2.40 equiv.), PEPPSI-IPr (10.0–15.0 mol%), 60 °C in THF; (D)  $\text{K}_4[\text{Fe}(\text{CN})_6] \cdot 3\text{H}_2\text{O}$  (0.250–5.00 equiv.), PEPPSI-IPr (5.00–20.0 mol%),  $\text{Na}_2\text{CO}_3$  (2.50–5.00 equiv.), 160 °C in DMF; (E) (I)  $^n\text{BuLi}$  (2.40 equiv.), TMEDA (2.40 equiv.), –78 °C in THF and (II) methanol (10.0 equiv.), –78–22 °C in THF.



dithiophene.<sup>7</sup> At the same time the functional group tolerance is significantly lower. Whilst the *ortho*-substituted anilines transform to the desired products, the *ortho,ortho'*-disubstituted anilines only couple efficiently when halogenated anilines are selected. For establishing a broad substance library with a spectrum of electron donating to electron accepting substituents, alternative ways of functionalization need to be explored. On the one hand, synthesis of *anti-anti*-3,9-dibrominated BBTs **4** via Buchwald–Hartwig amination, starting from the respective tetrabrominated sulfane **2** with BINAP as a ligand, transforms electron-rich anilines. Following this up by a sequence of bromine-lithium exchange with <sup>n</sup>BuLi and quenching with methanol reliably yields the desired products **3** with a plain BBT's scaffold.<sup>4a</sup> On the other hand, activation of C–Cl bonds on BBTs with chlorinated *N*-aryl moieties can be established. The NHC–Pd-catalyst Peppsi<sup>TM</sup>–IPr reliably promotes cyanation as well as Kumada coupling with a Grignard reagent. Since the synthesis of **3a** with directly employing *ortho*-cyanoaniline was previously known to result in a poor yield of 5%, the herein-reported two-step synthesis with an overall yield of 27% can be seen as an improved and more reliable alternative.<sup>4b</sup>

### Crystal data – molecular structure and underlying crystal packing patterns

Most herein-synthesized BBTs **3** and **4** were extensively characterized by X-ray diffraction experiments elucidating BBT's molecular structures (Fig. 4). They are hereafter best quantified by their *S,N*-folding, torsion, and *S–N–C<sub>aryl</sub>* angles (see ESI: Chapter S3.1†). All BBTs adopt an *N-intra* conformation with an almost orthogonally twisted *N*-aryl moiety with respect to the BBT's backbone, resulting torsion angles of ~0°. *S,N*-folding angles fall in a range from 146 to 180°, whilst *S–N–C<sub>aryl</sub>*-angles rise from 141° to a complete extension of the *N*-aryl moiety to the *S,N*-axis with 180°. Compared to their computational minimum geometries overall a strong induced planarization of BBTs' backbone upon crystallization is

apparent (B3LYP/6-311++G\*\*). The presence of two molecules per asymmetric unit for **3**, as for **3e**, **3f**, and **3r**, generally seems to lead to a more pronounced butterfly structure. In addition, **3f** is found with three different polymorphs, showing the overall most folded structure even if there is only a single molecule in the asymmetric unit.

The BBTs **3o**, **3p**, **3r**, and **4b** with a heterogenic substitution pattern reveal cocrystallization of both possible *N-intra* conformers. This indicates that the DFT predicted *N-intra-intra* equilibration of conformation in solution is present. The computationally obtained difference of Gibbs free energy  $\Delta G$  of the *N-intra* conformers can be extrapolated. By calculating the corresponding equilibrium constant *K*, the relative ratio of both *N-intra* conformers to each other can be determined. Furthermore, the planar transition state of ring inversion is computed for **3a–e** and all homogeneously substituted derivatives **3f**, **3g**, **3h**, **3i**, **3j**, and **4d**, opening up for extraction of the rate constant *k* of this *N-intra-intra* equilibration. The small free activation energies  $\Delta G_A^\ddagger$  below 2.0 kcal mol<sup>–1</sup> and resulting high rate constants *k* in the order of 10<sup>11</sup>–10<sup>12</sup> s<sup>–1</sup> suggest, that a substantial free ring inversion is very likely (see ESI: Chapter S4.2†). Measured NMR spectra prove this experimentally by displaying only a single set of signals. In order to possibly gain an understanding of the induced planarization in the crystalline state, the crystal packing patterns superimposed on the individual molecule's geometry are examined in more detail (see ESI: Chapter S3.2†). A structurally similar crystal packing pattern is found for the derivatives with only one molecule per asymmetric unit and an *ortho*-substitution pattern (**3a–d**) excepted **3c**, a homogeneous *ortho,ortho'*-substitution pattern (**3f**, **3g**, **3h**, **3i**, **3j**), and also for the heterogeneously substituted derivatives **3p** and **3t**. The single molecules form staircase-like structures with an overlap of approximately a half of the BBTs' backbones. For structures **3a** and **3g–3j**, a larger overlap results solely from the offset of the individual molecules in a self-defined *y*-axis, whereas for **3b**, **3d** and **3f** the overlap is reduced by additional offset in the self-defined *x*-ordinate. The molecules of one staircase are aligned in the same direction, which means that the *N*-aryl moieties all face the same side. These superordinate staircase-like structures are usually not consistently aligned parallel across the entire crystal but are rather twisted with respect to each other. The degree of twisting depends on the compound. Only for molecule **3j** a parallel orientation of the staircase-like substructures relative to each other is adopted. This places the BBTs' backbones as well as the 90°-twisted *N*-aryl moieties each in alignment. The crystal packing patterns of **4a**, **4b**, and **4d** do not significantly differ in their degree of planarization despite the varying number of molecules per asymmetric unit, unlike those of BBTs **3**. With their maximized folding angles and *S–N–C<sub>aryl</sub>*-angles of up to 180° 3,9-dibrominated BBTs **4** even outshine BBTs **3** by achieving full planarization. They also exhibit a half-sided overlap of the BBTs' backbones with only offset in the self-defined *y*-axis. This overlap is maximized by the two bromine atoms extending the BBT's backbone causing a stronger planarization. The *N*-aryl moieties of the

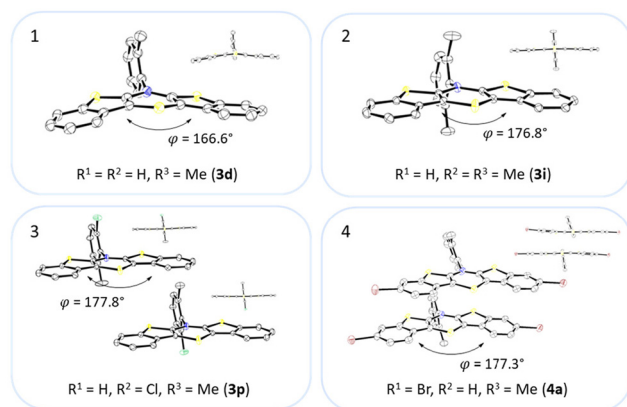


**Fig. 4** Molecular structures of **3d** (1), **3i** (2), **3p** (3) and **4a** (4). The thermal ellipsoids are set at a 50% probability level while all hydrogen atoms are omitted for clarity.





individual molecules are again oriented in the same direction. The staircase-like substructures are not twisted relative to each other but arranged alternately parallel as for **3j**. To better illustrate the arrangement with regards to the twisting of the staircase-like substructures relative to one another, the structure of compounds **3d**, **3i**, and **4a** are exemplarily compared in Fig. 5.

For all above-described crystal packing patterns the intermolecular distance of the planarized BBTTs' backbones of two individual molecules is  $\sim 3.38$  to  $4.13$  Å. This lies just around the van der Waals radii of two carbon atoms with  $3.40$  Å.<sup>8</sup> Only for structure **3a** an even stronger proximity of the BBTT scaffolds occurs with values of  $3.34$  to  $3.49$  Å, resulting in the beginning of  $\pi$ - $\pi$ -stacking (Fig. 6). The shortest C-C contact of  $3.369$  Å arises between two carbon atoms of the anellated benzenes of neighboring BBTT's backbones. Corresponding Hirshfeld surface analysis also depicts this, especially the C-C contact coded for in red. The corresponding fingerprint diagrams reflect this by their light blue areas in the range from  $1.8$ – $2.0$   $d_i$  to  $1.8$ – $2.0$   $d_e$ .<sup>9</sup> Resultingly, the planar geometry and the extent of the intermolecular proximity of the BBTTs' single molecules can be positively assessed with regard to a possible application as an OSC. Material science knows that a sufficient electronic coupling arises from intermolecular distances of around  $3.4$  to  $4.0$  Å, as a basis for potential charge carrier mobility.<sup>10</sup> Comparable thiophene-acene based materials with intermolecular distances of around  $3.52$  and  $3.56$  Å show

decent charge carrier mobility.<sup>11</sup> The remaining derivatives of **3** show no consistent packing patterns. The still quite planarized derivatives **3o** and **3n** with folding angles of  $165^\circ$  at least show the presence of a substructure, described herein as a pair-like arrangement. The individual molecules are rotated by  $180^\circ$  relative to each other, whereby their *N*-aryl moieties are oriented in opposite directions. At the same time, the BBTT's scaffolds overlap again halfway. A similar pair-like arrangement, but with a stronger overlap, could be identified for the *para*-aryl congeners with a pronounced planarization in their molecular structure.<sup>4c</sup>

### Antiaromaticity

An investigation whether the herein presented planarized BBTTs also exhibit antiaromaticity of the central 1,4-thiazine has to be scrutinized. BBTTs with folding angles over  $177^\circ$  can be analyzed by the well-established DFT-procedure of computing nuclear independent chemical shifts (NICS) using the crystal data's geometry as an input (B3LYP/6-311+G\*\*).<sup>12</sup> Therefore, BBTTs **3a**, **3g**, **3p**, **3h**, **3i**, **4a**, **4b**, and **4d** are examined by placing ghost atoms in the center and  $1$  Å above and below the plane, of each respective ring, providing the NICS<sub>iso</sub>(0) and NICS<sub>iso</sub>(+1/−1) values of interest. The outcome clearly reveals diatropic ring currents for the ring systems of the fused benzo[*b*]thiophenes and thus, as expected, indicates their aromaticity. The central 1,4-thiazine rings, however, each

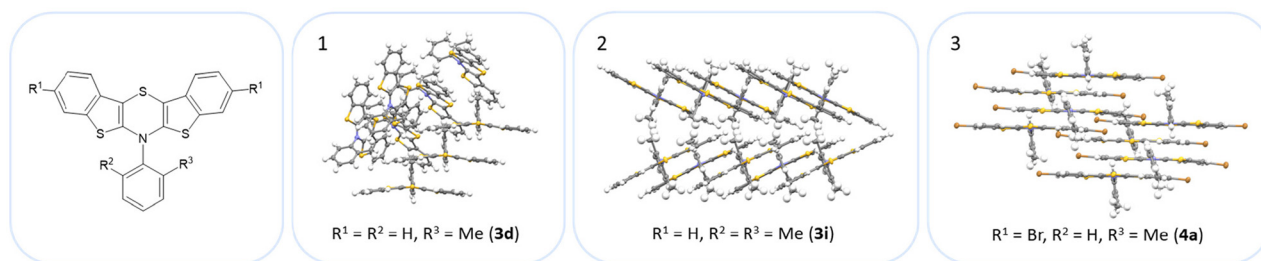


Fig. 5 Illustration of the twisting of the staircase-like substructures using the example of **3d** (1), **3i** (2) and **4a** (3).

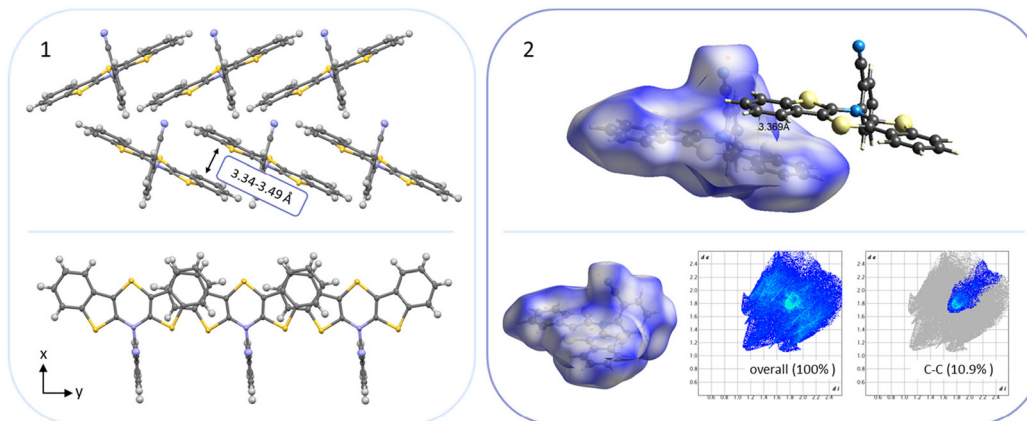


Fig. 6 (1) Section of the crystal packing pattern of *anti-anti-N-ortho*-cyanophenyl-BBTT **3a**. (2) Graphical depiction of the shortest C-C-contact between two BBTT single molecules of one staircase-like substructure as well as the Hirshfeld surface with their respective fingerprint diagrams.



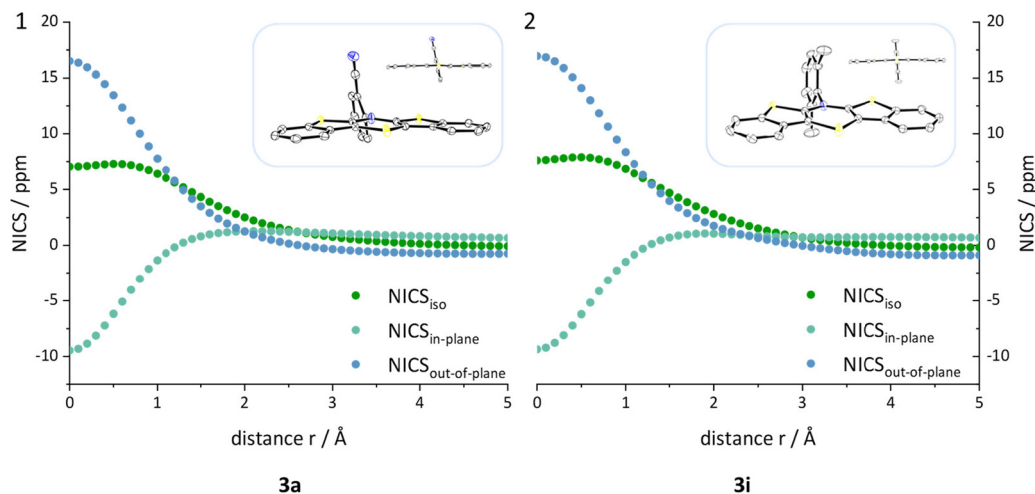


Fig. 7  $NICS_{iso}$ ,  $NICS_{in-plane}$  and  $NICS_{out-of-plane}$  values plotted against the distance  $r$  of the ghost atom from the center of the 1,4-thiazine as well as the underlying crystal structure geometry exemplarily for **3a** (1) and **3i** (2) (B3LYP/6-311+G\*\*).

exhibit a paratropic ring current, which suggests that those rings are antiaromatic. This is further supported by an in-depth analysis, in which the  $NICS_{iso}$  value, divided into its underlying  $NICS_{in-plane}$  and  $NICS_{out-of-plane}$  contributions, is calculated. The ghost atoms are hence placed starting from in the centroid to 5 Å above the 1,4-thiazine ring. The plotted curves, e.g. see Fig. 7, clearly indicate that the 1,4-thiazine rings are not nonaromatic but rather possess considerable antiaromatic character (see ESI: Chapter S3.3†).

### Optoelectronic properties and electronic structure

The optoelectronic properties of BBTTs **3** are assessed *via* cyclic voltammetry for the ground state and UV/vis absorption and emission spectroscopy for the excited state elucidating the electronic structure (Table 1). Spectroelectrochemistry is used to generate the oxidized species and to characterize their UV/vis absorption behavior. A deeper insight is gained by accompanying computational studies employing Gaussian 09 for (TD)-DFT-calculations.<sup>13</sup>

All cyclic voltammograms (CVs) of BBTTs **3** reveal a three-stage redox system of Weitz type with two clearly separated redox processes,<sup>14</sup> which are caused by consecutive one-electron transitions with Nernstian reversibility (Fig. 8).

According to their electronic nature, electron donating substituents shift the first redox potential  $E_0^{0/+1}$  to lower potentials, whereas electron accepting substituents shift the redox potential anodically in comparison to the plain BBTT **5**. Compared to their *para*-congeners the first redox potentials  $E_0^{0/+1}$  generally appear in the same range, but *ortho*-substituents show a stronger influence on the shift of the redox potentials  $E$ .<sup>4b,c</sup> This can be explained by an increase of the inductive and mesomeric substituent effects when considering a shortening of the bond length between the carbon atom and the fused substituent. This results as a consequence of the constitutional change from *para*- to *ortho*-substitution as supported computationally (B3LYP/6-311++G\*\*). And this further

accounts for the unexpected larger anodic shift caused by the fluorine over the chlorine substitution, since halogens are the only substituents inheriting a dominant inductive effect.<sup>15</sup> Upon bond contraction the inductive effect of fluorine, due to the more pronounced electronegativity,<sup>16</sup> becomes significantly more dominant than for chlorine. This rationalizes the overall stronger shifted potentials. The second redox potentials  $E_0^{+1/+2}$  of **3** also demonstrate the same dependency of the potential shift to the electronic nature of the substituent. At the same time these are overall progressively anodically shifted along with increasing steric congestion due to a change from *para*-<sup>4c</sup> to *ortho*- and to *ortho,ortho'*-substitution pattern. These anodic shifts fall within the order of ~70 mV for each constitutional change. Due to this consistency, prediction of the redox potentials  $E_0^{0/+1}$  and  $E_0^{+1/+2}$  of *anti-anti-N-ortho,ortho'*-disubstituted phenyl-BBTTs **3f-t** by their *ortho*-analogues **3a-e** is possible (see ESI: Chapter S4.4.2†). To the absolute redox potential  $E_0$  of the plain *anti-anti-N*-phenyl BBTT **5** are added the two differences in redox potentials  $\Delta E$  of the *ortho*-derivatives **3a-e** bearing the substituents of interest to the redox potential  $E$  of **5** as increments. Linear regression analysis with the experimentally determined redox potentials yields very satisfactory regression coefficients ( $r^2 = 0.992$  and  $0.973$ ). This indicates a consistent and therefore intrinsic effect of the introduction of both *ortho*-substituents on the electronic structure, even though the geometric structure is mainly affected by the introduction of the second *ortho*-substituent. The anodic shift of the second redox potentials  $E_0^{+1/+2}$  furthermore consequently leads to enlarged semiquinone formation constants  $K_{sem}$ .<sup>14a</sup> Those fall in orders of magnitude of  $10^{13}$  for *ortho*- and up to  $10^{13}$ – $10^{15}$  for *ortho,ortho'*-derivatives. Their *para*-congeners show lower values of  $K_{sem}$  with  $10^{11}$ – $10^{13}$ .<sup>4a,c</sup> This unambiguously points out an increase in relative thermodynamic stability of the formed radical cations by the progressively sterically more demanding substitution patterns. The increasing radical stabilization is additionally supported com-



**Table 1** Electrochemical and photophysical properties of BBTs **3** and **4** (redox potentials  $E_0$  (vs.  $\text{Fc}/\text{Fc}^+ = 0.00$  V) and UV/vis data recorded in  $\text{CH}_2\text{Cl}_2$ , 298 K)

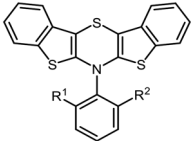
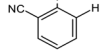
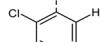
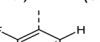
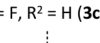
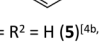
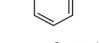
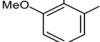
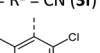
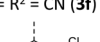
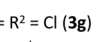
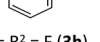
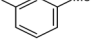
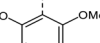
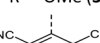
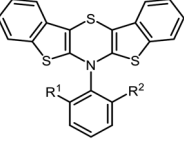
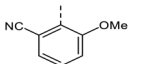
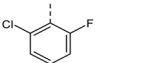
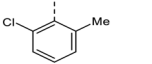
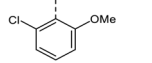
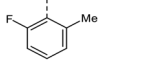
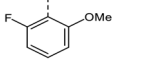
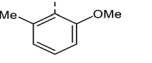
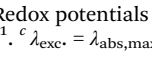
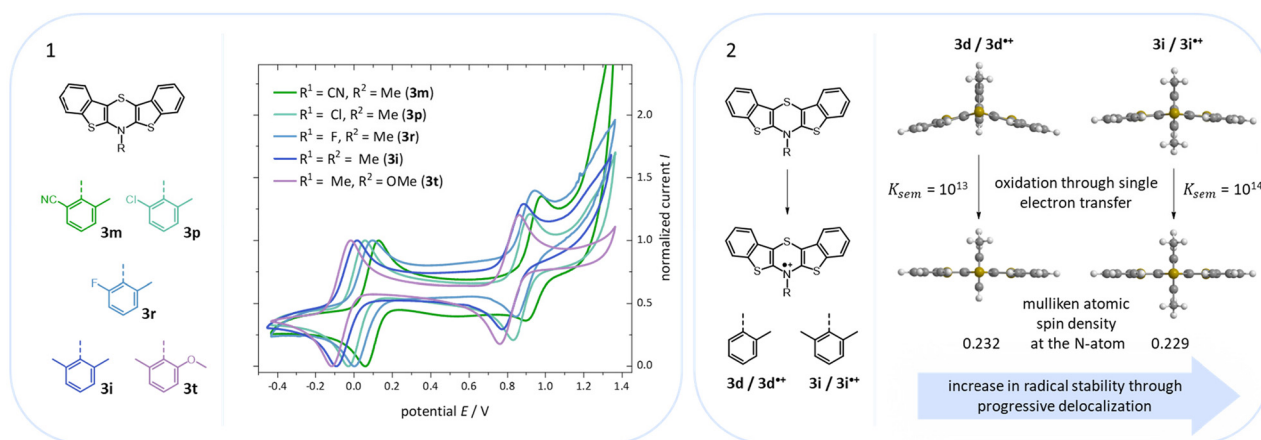
 $E_0^{0/+1}, {}^a$ mV $(E_0^{0/+1}, {}^b$ mV)	$E_0^{+1/+2}, {}^a$ mV $(E_0^{+1/+2}, {}^b$ mV)	$K_{\text{Sem}}$	$\lambda_{\text{abs, sol}}, \text{nm}$ $(\epsilon, 10^3 \text{ L mol}^{-1} \text{ cm}^{-1})$	$\lambda_{\text{em, sol}}, {}^c$ nm $(\Delta\epsilon, \text{cm}^{-1}/\Phi/\tau, {}^d$ $\text{ns}/k_r, \text{s}^{-1}/k_{\text{nr}}, \text{s}^{-1})$	$\lambda_{\text{abs, pow}}, {}^e$ $\text{nm}$	$\lambda_{\text{em, pow}}, {}^e$ $\text{nm} (\Phi)$
 $\text{R}^1 = \text{CN}, \text{R}^2 = \text{H}$ ( <b>3a</b> ) <sup>[4b]</sup>	115 (119)	895 (906)	$1.65 \times 10^{13}$	233 (44.3), 309 (6.2), 411 (2.9)	519, 543 (5900/0.00/ n.d./n.d./n.d.)	417 620 (0.00)
 $\text{R}^1 = \text{Cl}, \text{R}^2 = \text{H}$ ( <b>3b</b> ) <sup>[4b]</sup>	20 (33)	828 (840)	$4.42 \times 10^{13}$	235 (54.2), 263 (25.1, sh), 314 (10.2), 423 (3.6)	519, 540 (5100/0.06/ $3.31/1.81 \times 10^7/2.84 \times 10^8$ )	420 546 (0.04)
 $\text{R}^1 = \text{F}, \text{R}^2 = \text{H}$ ( <b>3c</b> )	49 (58)	848 (865)	$3.44 \times 10^{13}$	234 (49.5), 267 (20.8, sh), 282 (13.3, sh), 315 (7.4), 418 (3.1)	515 (sh), 539 (5400/0.20/ $8.67/2.31 \times 10^7/9.23 \times 10^7$ )	422 543 (0.36)
 $\text{R}^1 = \text{H}, \text{R}^2 = \text{H}$ ( <b>3d</b> )	−22 (−18)	734 (742)	$7.61 \times 10^{12}$	236 (46.3), 268 (19.4, sh), 321 (7.6), 425 (3.5)	526, 548 (5300/0.16/ $9.18/1.74 \times 10^7/9.15 \times 10^7$ )	414 567 (0.09)
 $\text{R}^1 = \text{Me}, \text{R}^2 = \text{H}$ ( <b>3e</b> )	−29 (−23)	766 (771)	$2.92 \times 10^{13}$	234 (50.3), 269 (21.1, sh), 316 (9.0), 429 (4.0)	525, 551 (5200/0.24/10.6/ $2.27 \times 10^7/7.20 \times 10^7$ )	433 582 (0.06)
 $\text{R}^1 = \text{MeO}, \text{R}^2 = \text{H}$ ( <b>3f</b> )	−69 (−63)	748 (761)	$6.97 \times 10^{13}$	232 (65.3), 270 (27.6), 318 (10.3), 425 (4.7)	521, 547 (5200/0.22/ $10.3/2.13 \times 10^7/7.55 \times 10^7$ )	429 551 (0.09)
 $\text{R}^1 = \text{CN}, \text{R}^2 = \text{CN}$ ( <b>3g</b> )	261 (256)	1066 (1073)	$4.41 \times 10^{13}$	232 (67.3), 251 (33.0, sh), 260 (25.9, sh), 300 (12.0, sh), 411 (2.5)	—	410 —
 $\text{R}^1 = \text{Cl}, \text{R}^2 = \text{Cl}$ ( <b>3h</b> )	83 (93)	926 (951)	$1.92 \times 10^{14}$	230 (57.5), 264 (24.7, sh), 310 (8.8), 420 (3.4)	509, 536 (sh) (5200/ 0.00/n.d./n.d./n.d.)	440 —
 $\text{R}^1 = \text{F}, \text{R}^2 = \text{F}$ ( <b>3i</b> )	139 (143)	946 (982)	$4.81 \times 10^{13}$	234 (49.5), 265 (21.5, sh), 279 (14.9, sh), 309 (8.2), 413 (3.3)	511 (sh), 529 (5300/ 0.00/n.d./n.d./n.d.)	418 532 (0.01)
 $\text{R}^1 = \text{Me}, \text{R}^2 = \text{Me}$ ( <b>3j</b> )	−46 (−35)	819 (835)	$4.57 \times 10^{14}$	233 (52.8), 269 (22.9), 316 (8.5), 434 (4.4)	524, 553 (5000/0.27/11.2/ $2.42 \times 10^7/6.53 \times 10^7$ )	439 562 (0.18)
 $\text{R}^1 = \text{MeO}, \text{R}^2 = \text{MeO}$ ( <b>3k</b> )	−97 (−89)	789 (787)	$1.05 \times 10^{15}$	236 (53.4), 270 (22.6, sh), 315 (11.1), 429 (3.6)	518, 544 (4900/0.33/10.5/ $3.13 \times 10^7/6.36 \times 10^7$ )	438 588 (0.18)
 $\text{R}^1 = \text{CN}, \text{R}^2 = \text{Cl}$ ( <b>3l</b> )	156 (156)	1014 (1019)	$3.47 \times 10^{14}$	231 (73.6), 250 (35.9, sh), 279 (18.5, sh), 315 (9.3, sh), 413 (3.3)	—	414 —
 $\text{R}^1 = \text{CN}, \text{R}^2 = \text{F}$ ( <b>3m</b> )	182 (185)	1006 (1014)	$9.12 \times 10^{13}$	231 (60.9), 248 (36.3, sh), 277 (17.8, sh), 316 (7.6, sh), 412 (2.9)	—	416 —
 $\text{R}^1 = \text{CN}, \text{R}^2 = \text{Me}$ ( <b>3n</b> )	100 (102)	952 (956)	$2.72 \times 10^{14}$	231 (58.2), 268 (21.3, sh), 308 (7.9), 419 (3.3)	—	427 —



Table 1 (Contd.)

	$E_0^{0/+1},^a$ mV ( $E_0^{0/+1},^b$ mV)	$E_0^{+1/+2},^a$ mV ( $E_0^{+1/+2},^b$ mV)	$K_{Sem}$	$\lambda_{abs,sol},$ nm ( $\epsilon, 10^3$ L mol $^{-1}$ cm $^{-1}$ )	$\lambda_{em,sol},^c$ nm ( $\Delta\nu, \text{cm}^{-1}/\Phi/\tau,^d$ ns/ $k_r, \text{s}^{-1}/k_{nr}, \text{s}^{-1}$ )	$\lambda_{abs,pow},^e$ nm	$\lambda_{em,pow},^e$ nm ( $\Phi$ )
 $R^1 = \text{CN}, R^2 = \text{OMe}$ ( <b>3m</b> )	66 (81)	925 (948)	$3.61 \times 10^{14}$	232 (62.0), 267 (22.6, sh), 304 (15.0), 413 (3.9)	—	420	—
 $R^1 = \text{Cl}, R^2 = \text{F}$ ( <b>3p</b> )	108 (111)	940 (954)	$1.24 \times 10^{14}$	233 (40.7), 265 (17.8, sh), 282 (10.9, sh), 308 (6.9), 413 (2.90)	511 (sh), 525 (5200/ 0.00/n.d./n.d./n.d.)	420	534 (0.00)
 $R^1 = \text{Cl}, R^2 = \text{Me}$ ( <b>3r</b> )	28 (31)	882 (894)	$2.90 \times 10^{14}$	234 (57.0), 271 (23.5), 316 (8.1), 433 (4.1)	516, 544 (4700/0.16/ 7.23/2.21 $\times 10^7$ /1.16 $\times 10^8$ )	431	552 (0.09)
 $R^1 = \text{Cl}, R^2 = \text{OMe}$ ( <b>3i</b> )	7 (6)	871 (874)	$4.48 \times 10^{14}$	233 (56.7), 267 (24.4), 310 (8.7), 423 (4.0)	513, 539 (5100/0.03/ 8.92/3.36 $\times 10^6$ /1.09 $\times 10^8$ )	425	544 (0.02)
 $R^1 = \text{F}, R^2 = \text{Me}$ ( <b>3t</b> )	51 (56)	875 (893)	$9.16 \times 10^{13}$	233 (45.0), 269 (18.7, sh), 282 (12.9, sh), 312 (7.1), 424 (3.2)	515, 541 (5100/0.19/ 10.7/1.77 $\times 10^7$ /7.55 $\times 10^7$ )	431	543 (0.05)
 $R^1 = \text{F}, R^2 = \text{OMe}$ ( <b>3r</b> )	12 (15)	860 (873)	$2.35 \times 10^{14}$	233 (57.4), 269 (24.8), 312 (8.9), 416 (4.0)	515 (sh), 535 (5300/0.11/ 7.00/1.57 $\times 10^7$ /1.27 $\times 10^8$ )	425	575 (0.12)
 $R^1 = \text{F}, R^2 = \text{OMe}$ ( <b>3s</b> )	−61 (−56)	804 (818)	$4.59 \times 10^{14}$	234 (97.1), 271 (43.6), 312 (15.2), 430 (7.7)	519, 549 (5000/0.33/11.2/ 2.94 $\times 10^7$ /5.98 $\times 10^7$ )	433	554 (0.28)
 $R^1 = \text{Me}, R^2 = \text{OMe}$ ( <b>3t</b> )							

<sup>a</sup> Redox potentials obtained by extrapolation of data with  $\nu = 100, 250, 500$ , and  $1000 \text{ mV s}^{-1}$  to  $\nu = 0.00 \text{ mV s}^{-1}$ . <sup>b</sup> Redox potentials at  $\nu = 100 \text{ mV s}^{-1}$ . <sup>c</sup>  $\lambda_{exc} = \lambda_{abs,max,sol}$ . <sup>d</sup> Lifetime  $\tau$  measured at  $\lambda_{exc} = 448.8 \text{ nm}$ . <sup>e</sup> Powder samples measured.



**Fig. 8** (1) CVs of BBTs of **3m**, **3p**, **3r**, **3i**, and **3t** (CVs recorded in  $\text{CH}_2\text{Cl}_2$ ,  $T = 298 \text{ K}$ ,  $0.1 \text{ M } [\text{nBu}_4\text{N}][\text{PF}_6]$ ,  $\nu = 100 \text{ mV s}^{-1}$ , Pt-working- und counter electrode, Ag/AgCl(3 M)-reference electrode, referenced with decamethylferrocene (DMFc)/DMFc $^+$ , potential vs. Fc/Fc $^+$  = 0.00 V). (2) Minimum geometries of BBTs **3d** and **3i** as well as their corresponding radical cations **3d** $^{+\bullet}$  and **3i** $^{+\bullet}$  ((u)B3LYP/6-311++G\*\*, IEFPCM  $\text{CH}_2\text{Cl}_2$ ) and illustration of the increase in the radical stability.

putationally by the manifestation of a stronger delocalization of the unpaired electron for the radical cations ((u)B3LYP/6-311++G\*\*). Whilst visualization of the spin density distribution

does not clearly illustrate this directly, the Mulliken atomic spin densities support this rationale. In accordance with the constitutional changes overall decreasing values on the central





1,4-thiazine core occur, while the values for the carbon atoms of the anellated benzo rings increase (see ESI: Chapter 4.2<sup>‡</sup>). Quantum chemistry also allows for calculation of the first redox potentials  $E_0^{0/+1}$  accounting for properties of native and oxidized species at the same time. The method is based on the free energy cycle, employing the thermodynamic data provided by calculation of BBTT's minimum geometries of the native species and the oxidized radical cation in gas phase and under SMD variation for computing  $\Delta G$  of solvation ((u)B3LYP/6-311++G\*\*, see ESI: Chapter 4.4.1<sup>‡</sup>).<sup>17</sup> The best correlations of the experimental and theoretical first redox potentials  $E_0^{0/+1}$  originate when, in case of a heterogenic substitution pattern, both possible theoretical *N-intra* conformation's first redox potentials  $E_{0,cal}^{0/+1}$  are incorporated. Therefore, their relative ratio is calculated by their difference in Gibbs free enthalpies  $\Delta G$  (B3LYP/6-311++G\*\*). Overall, this leads to a good fit of the experimental to the computational data ( $r^2 = 0.951$ ).

### Spectroelectrochemistry

Additionally, a spectroelectrochemical measurement has been carried out on *anti-anti-N-ortho,ortho'*-dimethylphenyl BBTT **3i**. This reliably generates the corresponding radical cation **3i**<sup>•+</sup> by *in situ* oxidation through a steady increase of the applied potential (Fig. 9).<sup>4d,19</sup>

The occurrence of distinct isosbestic points in the UV/vis absorption spectra indicates, that the oxidation to the radical cation proceeds without accumulation of intermediates. The pronounced bathochromic shift of the absorption bands upon oxidation indicates a significant change in the electronic structure. This arises from the major geometry changes upon oxidation, leading the BBTT's butterfly structure of **3i** to fully planarize resulting the BBTT's backbone of **3i**<sup>•+</sup> to reveal a *S,N*-folding angle of 180°. This allows for an accompanied strong

delocalization of the unpaired electron. The stability of **3i**<sup>•+</sup> over the time scale of this experiment (~30 min) underpins the high thermodynamic radical stability, also with a significant kinetic persistence. The X-band EPR spectrum in CH<sub>2</sub>Cl<sub>2</sub> at room temperature proves the paramagnetic character. It presents a hyperfine coupling pattern of three equidistant lines, reflecting the coupling of the electron spin of the unpaired electron to the nuclear spin of the nitrogen nucleus ( $I(^{14}\text{N}) = 1$ ).<sup>18</sup> Furthermore, the *g*-factor of 2.0224 indicates the predominant localization of the unpaired electron on the nitrogen atom. Furthermore, lowering the applied potential successfully leads to the corresponding reduction to **3i**. The attempt to generate the corresponding dication *in situ* fails as a consequence of side reactions. This can be identified by the absence of newly appearing bathochromic bands and isosbestic points as well as an increase in intensity in the hypsochromic region (see ESI: Chapter 4.5<sup>‡</sup>). In contrast to the corresponding dications of their *para*-BBTTs, the dication **3i**<sup>2+</sup> lacks the necessary persistence under the experimental conditions.<sup>4d</sup>

### UV/vis absorption and emission spectroscopy

BBTTs **3** have been examined by UV/vis absorption and emission spectroscopy, since some of the yellowish to orange compounds display emission in solution and in the solid state (Fig. 10). All BBTTs **3** reveal similar positions of the absorption and emission maxima despite a variation of functionalization (Fig. 11).

TD-DFT calculations allow for a deeper understanding by assignment of the bands to their underlying transitions (PBE1PBE/6-311++G\*\*).<sup>20</sup> Therefore, exemplarily for BBTTs **3f**–**3t** the derivatives with a homogenic substitution pattern have been chosen. In the case of **3a**–**e** with two non-identical *N-intra*

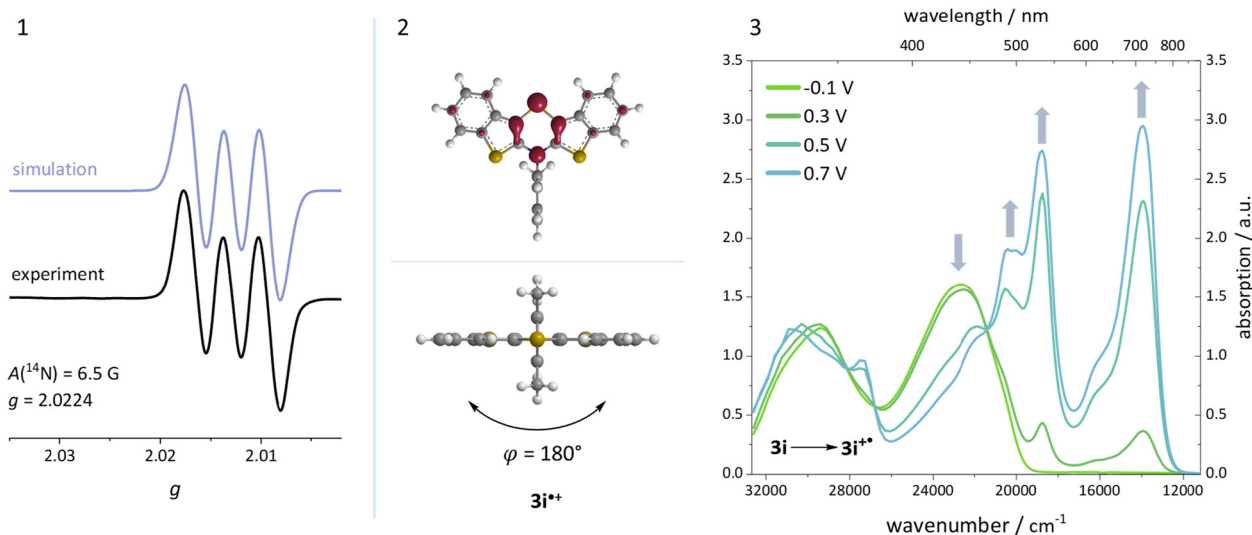


**Fig. 9** (1) EPR spectrum of radical cation **3i**<sup>•+</sup> (recorded in CH<sub>2</sub>Cl<sub>2</sub>, *T* = 298 K, *g*-factor referenced to external Mn<sup>2+</sup> in ZnS). (2) Visualization of the spin density distribution (B3LYP/6-311++G\*\*, IEFCM CH<sub>2</sub>Cl<sub>2</sub>, isosurface value 0.06 a.u.) and minimum geometry of **3i**<sup>•+</sup>. (3) Spectroelectrochemical measurement of **3i** to **3i**<sup>•+</sup> (recorded in CH<sub>2</sub>Cl<sub>2</sub>, *c* = 5 × 10<sup>-3</sup> M, *T* = 298 K, electrolyte 0.1 M [<sup>18</sup>Bu<sub>4</sub>N][PF<sub>6</sub>]; Pt-working electrode, GC-counter electrode and Ag-wire pseudo-reference electrode).



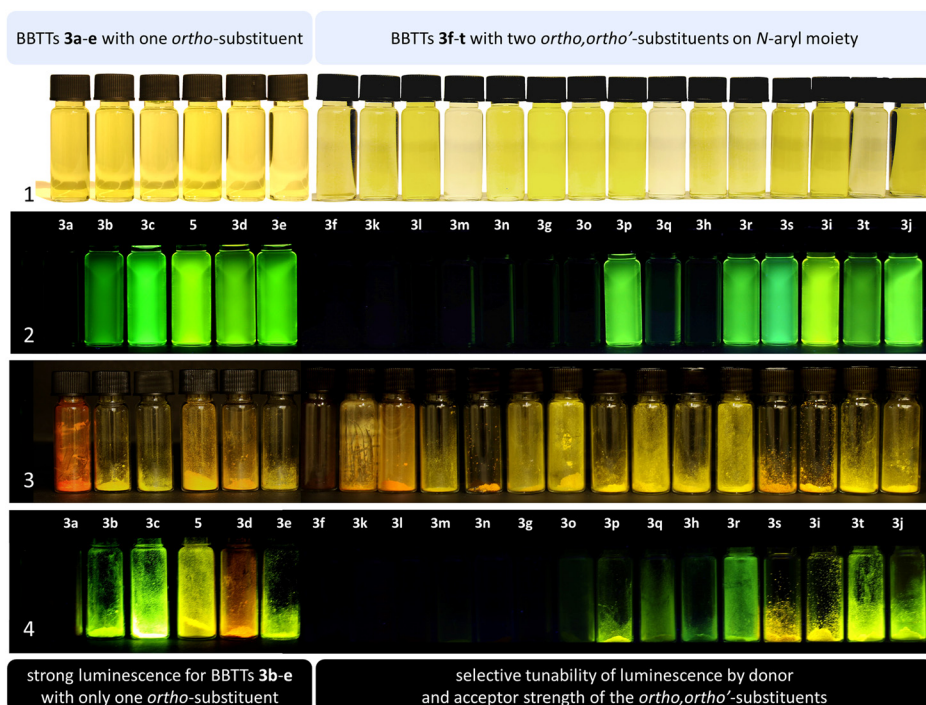


**Fig. 10** Solutions of BBTs **3** and **5** in  $\text{CH}_2\text{Cl}_2$  ( $T = 298 \text{ K}$ ,  $c = 10^{-4} \text{ M}$ ) at daylight (1) and under UV light (366 nm) (2). Powders of BBTs **3** and **5** ( $T = 298 \text{ K}$ ) at daylight (3) and under UV light (366 nm) (4).

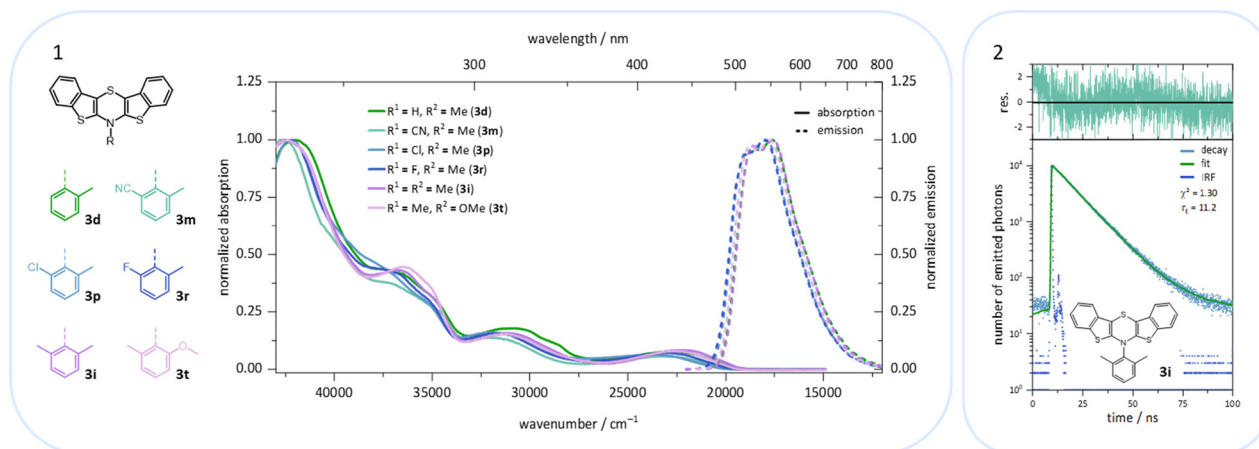


**Fig. 11** (1) UV/vis absorption and emission spectra of BBTs **3** in solution (recorded in  $\text{CH}_2\text{Cl}_2$ ,  $T = 298 \text{ K}$ ,  $c = 10^{-5}$  to  $10^{-7} \text{ M}$ ). (2) Lifetime data measured by TCSPC experiments exemplarily given for **3i**.

conformers, the thermodynamically favored one is considered (see ESI: Chapter 5.2<sup>†</sup>).

Calculations nicely underline the four experimentally seen dominant absorption bands. They reproduce their relative dropping intensities and extinction coefficients along the decreasing wavenumber by declining oscillator strengths well. The longest wavelength absorption bands occur overall at around 430 nm, indicating to originate from HOMO  $\rightarrow$  LUMO transitions for mostly all derivatives. Only for nitrile-bearing BBTs the transitions arise from the HOMO into orbitals ener-

getically higher than the LUMO. The consideration of DFT-computed Kohn–Sham frontier molecular orbitals suggests a plausible reason for the independency of the position of the absorption and emission bands from the substituent pattern. They reveal no coefficient density on the *ortho*-substituents of the *N*-aryls (Fig. 12). The transitions also show negligible charge transfer character, due to only a small shift of the coefficient density from the sole location on the central 1,4-thiazine (HOMO) to the delocalization over the whole BBT's backbone (LUMO) (see ESI: Chapter 5.2<sup>†</sup>).



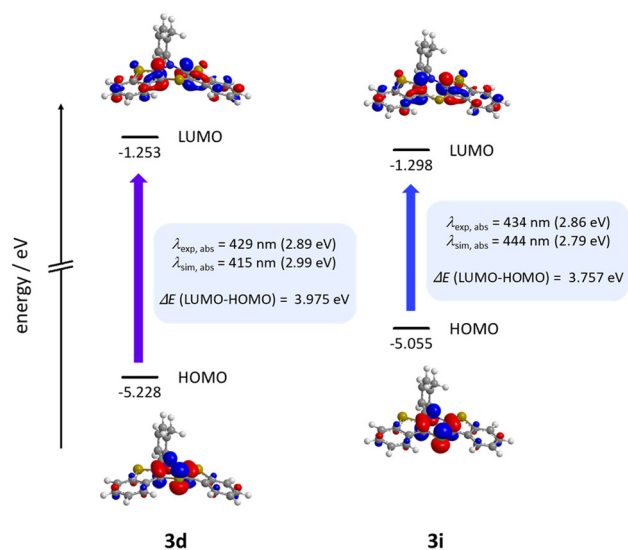


**Fig. 12** Selected Kohn-Sham frontier orbitals and their energies and the  $S_0$ - $S_1^*$ -transition of **3d** and **3i** (PBE1PBE/6-311++G\*\*, IEFPCM  $\text{CH}_2\text{Cl}_2$ , isosurface value at 0.05 a.u.).

The emission bands emerge at around 550 nm, excluding most nitrile-substituted BBTTs due to their indiscernible emission properties. They are best reproduced by TD-DFT calculations of the first singlet excited state ( $S_1$ ), indicating the emission to be fluorescence (Fig. 13). Fluorescence is experimentally proven by lifetime measurements *via* time-correlated single photon counting (TCSPC) experiments. They reveal a dependency of the lifetime  $\tau$  on an electron donating substituent, yielding the highest lifetimes  $\tau$  up to 11.2 (**3i**) (Fig. 11 and 2), 11.2 (**3t**), and 10.5 ns (**3j**) in solution. Additionally, the fluorescence quantum yields  $\Phi$  also display the same qualitative trend amounting up to 0.27 (**3i**), 0.33 (**3t**), and 0.33 (**3j**) in solution and 0.18 (**3i**), 0.28 (**3t**), and 0.18 (**3j**) in solid state for donor substituted BBTTs. From fluorescence quantum yields  $\Phi$  and lifetimes  $\tau$ , radiative rate constants  $k_r$  in a range from  $3.36 \times 10^6$  to  $3.13 \times 10^7 \text{ s}^{-1}$  and non-radiative rate constants  $k_{nr}$  in a range from  $5.98 \times 10^7$  to  $2.84 \times 10^8 \text{ s}^{-1}$  can be deduced. Consequently, it is found that non-radiative processes depopulate the excited state faster than radiative processes for all compounds. The examination of the spectroscopic data also allows for further discussion of the intended suppression of the butterfly structure. Therefore, the Stokes shifts  $\Delta\tilde{\nu}$  are taken into consideration. These range between 5100 to 5900  $\text{cm}^{-1}$  for the *ortho*-derivatives, and are thus comparable to their *para*-congeners.<sup>4c</sup> The *ortho,ortho'*-derivatives, on the other hand, show overall diminished Stokes shifts  $\Delta\tilde{\nu}$  of 4700 to 5300  $\text{cm}^{-1}$ . Considering that solvation effects have no significant influence on the absorption and emission maxima, and that the geometries of the vibrationally relaxed  $S_1$ -states of BBTTs **3** reveal uniformly planarized BBTT scaffolds with folding angles of  $\sim 180^\circ$ , the Stokes shifts  $\Delta\tilde{\nu}$  correlate with the extent of folding in the  $S_0$ -ground state. Consequently, the comparatively small Stokes shifts  $\Delta\tilde{\nu}$  of **3f-3t** account for smaller structural

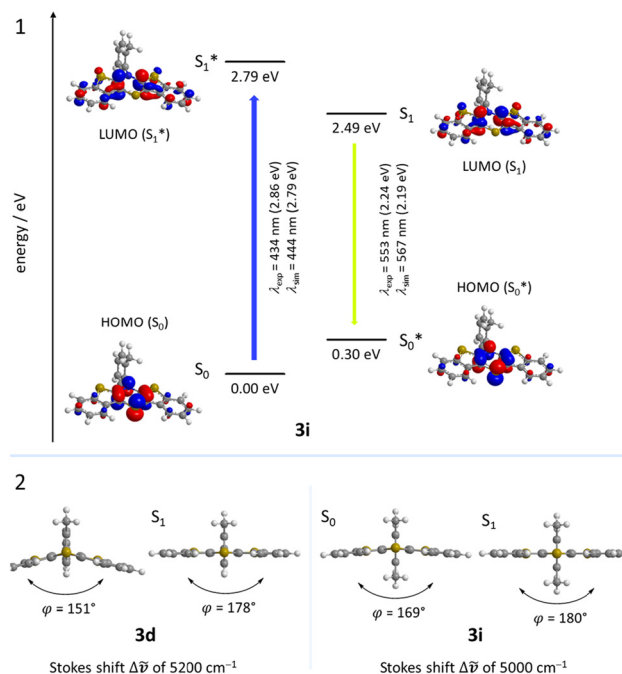


**Fig. 13** (1) TD-DFT calculated Jablonski diagram of BBTT **3i** with the associated Kohn-Sham frontier orbitals of the  $S_0$ - $S_1^*$ -transition and  $S_0^*$ - $S_1$ -transition. (2) Vibrational relaxed minimum  $S_0$ - and  $S_1$ -geometries of **3d** and **3i** indicated with their  $S,N$ -folding angles  $\phi$  and Stokes shifts  $\Delta\tilde{\nu}$  (PBE1PBE/6-311++G\*\*, IEFPCM  $\text{CH}_2\text{Cl}_2$ , isosurface value 0.05 a.u.).

changes upon photonic excitation. This clearly advocates for stronger planarized  $S_0$ -ground state geometries of the BBTTs **3f-t** bearing *ortho,ortho'*-disubstituted *N*-aryl moieties. The experimental observations reproduce overall well the computationally founded assumption that DFT calculated minimum geometries provide a good approximation of the conformation in solution.

## Conclusion

The computationally founded concept to force formally anti-aromatic BBTTs into a planarized conformation by introduction of a sterically restricting *ortho,ortho'*-substitution pattern on the *N*-aryl moiety can be synthetically successfully implemented by palladium-catalyzed cross-coupling methods. A substance library with a broad variety of electron donating to electron accepting substituents is readily obtained. X-ray analyses reveal the sole adoption of the *N-intra* conformation for BBTTs' molecular structures. The comparison to DFT-minimum geometries moreover indicates an overall induced planarization of BBTTs in the crystalline state. Maximized  $S,N$ -folding angles and  $S-N-C_{aryl}$ -angles up to almost  $180^\circ$  for compounds **3a-t** and **4a** and up to a full planarization for compounds **4b** and **4d** manifest. Therefore, examination of planarized BBTTs with NICS calculations clearly supports a considerable antiaromaticity of the central 1,4-thiazine. The superordinate crystal packing patterns furthermore mainly depict stair-



case-like substructures consisting of half-side overlapped BBTs' backbones with intermolecular C–C distances as low as 3.369 Å. Cyclic voltammetry depicts tunable and low first redox potentials  $E_0^{0/+1}$  at around –100 to 250 mV. The semiquinone formation constants  $K_{\text{sem}}$  indicate pronounced radical cation stabilities of BBTs **3**, that unambiguously exceed their *para*-analogues upon the change of constitution to *ortho*-substituents of around two orders of magnitude. This arises from an increased delocalization of the radicals over the BBTs' planarized backbones. This is substantiated by DFT calculations of the Mulliken atomic spin density as well as the strongly bathochromically shifted absorption bands of the *in situ* generated radical cation by spectroelectrochemistry. Photophysical studies of native compounds reveal intensive emission at around 550 nm upon photonic excitation with fluorescence quantum yields  $\Phi$  of up to 0.33 and lifetimes  $\tau$  in the range of 3–11 ns. The decreased Stokes shifts  $\Delta\tilde{\nu}$  of *ortho,ortho'*-derivatives compared to their *para*- and *ortho*-analogues hint at a successful sterically induced enlargement of the *S*,*N*-folding angles in the  $S_0$ -ground state. Therefore, the concept of conformationally planarized BBTs by the reduction of the butterfly folding holds even true in solution. The experiments are furthermore plausibly rationalized by (TD-)DFT calculations corroborating the electronic structure. In summary, synthesized BBTs can be considered as strong donor moieties, being reversible redox chromophores and tunable luminophores. Especially BBTs with the *ortho,ortho'*-substitution pattern outshine their *para*-congeners. The imposed steric strain seems to enforce planarization of BBTs, in the crystalline solid state as well as in solution. Furthermore, this modification promises a broader tunability of the redox potentials  $E_0$  as well as an increased impeccable radical cation stability. It also implements a selective tunability of the emission properties from intense to elusive fluorescence. Ultimately, due to their favorable properties, these BBT donors present potential for a further development leading to highly interesting more electron-rich substitutes for phenothiazines, especially for organo-electronic applications.

## Data availability

The data supporting this article have been included as part of the ESI.†

Crystallographic data: deposition numbers CCDC 2346002 (for **3a**), 2345988 (for **3b**), 2345990 (for **3c**), 2345982 (for **3d**), 2345989 (for **3e**), 2345999 (for **3f** (polymorph I)), 2345994 (for **3f** (polymorph II)), 2345996 (for **3f** (polymorph III)), 2335542 (for **3g**), 2335553 (for **3h**), 2345957 (for **3i**), 2345956 (for **3j**), 2345983 (for **3k**), 2345987 (for **3l**), 2345959 (for **3m**), 2345998 (for **3n**), 2345948 (for **3o**), 2345958 (for **3p**), 2345985 (for **3r**), 2345992 (for **3t**), 2345944 (for **4a**), 2346000 (for **4b**), and 2345986 (for **4d**) contain the supplementary crystallographic data for this paper.‡ These data are provided free of charge by the joint Cambridge Crystallographic Data Centre and Fachinformationszentrum Karlsruhe Access Structures service.

## Conflicts of interest

There are no conflicts to declare.

## References

- 1 S. Ahmad, Organic semiconductors for device applications: current trends and future prospects, *J. Polym. Eng.*, 2014, **34**, 279–338.
- 2 (a) Q. Zhang, W. Hu, H. Sirringhaus and K. Müllen, Recent Progress in Emerging Organic Semiconductors, *Adv. Mater.*, 2022, **34**, 2108701; (b) Y. Shirota and H. Kageyama, *Chem. Rev.*, 2007, **107**, 953; (c) *Functional Organic Materials – Synthesis, Strategies, and Applications*, ed. T. J. J. Müller and U. H. F. Bunz, Wiley-VCH, Weinheim, 2007.
- 3 H. R. V. Berens and T. J. J. Müller, *S,N*-Heteropentacenes – Syntheses of Electron-Rich Anellated Pentacycles, *Org. Mater.*, 2021, **3**, 155–167.
- 4 (a) H. R. V. Berens, K. Mohammad, G. J. Reiss and T. J. J. Müller, 3,9-Disubstituted Bis[1]benzothieno[3,2-*b*;2',3'-*e*],[1,4]thiazines with Low Oxidation Potentials and Enhanced Emission, *J. Org. Chem.*, 2021, **86**, 8000–8014; (b) A. P. W. Schneeweis, S. T. Hauer, D. A. Lopez, B. von Dressler, G. J. Reiss and T. J. J. Müller, Game of Isomers: Bifurcation in the Catalytic Formation of Bis[1]benzothieno[1,4]thiazines with Conformation-Dependent Electronic Properties, *J. Org. Chem.*, 2019, **84**, 5582–5595; (c) A. P. W. Schneeweis, S. T. Hauer, G. J. Reiss and T. J. J. Müller, Bis[1]benzothieno[1,4]thiazines: Planarity, Enhanced Redox Activity and Luminescence by Thieno-Expansion of Phenothiazine, *Chem. – Eur. J.*, 2019, **25**, 3582–3590; (d) S. T. Hauer, A. P. W. Schneeweis, S. D. Waniek, L. P. Sorge, K. Heinze and T. J. J. Müller, Radical cations and dications of bis[1]benzothieno[1,4]thiazine isomers, *Org. Chem. Front.*, 2021, **8**, 5744–5755.
- 5 (a) A. D. Becke, Density-Functional Thermochemistry. III. The Role of Exact Exchange, *J. Chem. Phys.*, 1993, **98**, 5648–5652; (b) C. Lee, W. Yang and R. G. Parr, Development of the Colle-Salvetti correlation-energy formula into a functional of the electron density, *Phys. Rev. B: Condens. Matter Mater. Phys.*, 1988, **37**, 785–789; (c) R. Krishnan, J. S. Binkley, R. Seeger and J. A. Pople, Self-consistent molecular orbital methods. XX. A basis set for correlated wave functions, *J. Chem. Phys.*, 1980, **72**, 650–654; (d) A. D. McLean and G. S. Chandler, Contracted Gaussian basis sets for molecular calculations. I. Second row atoms, Z=11–18, *J. Chem. Phys.*, 1980, **72**, 5639–5648; (e) M. J. Frisch, J. A. Pople and J. S. Binkley, Self-consistent molecular orbital methods 25. Supplementary functions for Gaussian basis sets, *J. Chem. Phys.*, 1984, **80**, 3265–3269; (f) T. Clark, J. Chandrasekhar, G. W. Spitznagel and P. V. R. Schleyer, Efficient diffuse function-augmented basis sets for anion calculations. III.† The 3-21+G basis set for first-row elements, Li–F, *J. Comput. Chem.*, 1983, **4**, 294–301; (g) G. Scalmani and M. J. Frisch, Continuous surface





- charge polarizable continuum models of solvation. I. General formalism, *J. Chem. Phys.*, 2010, **132**, 114110.
- 6 (a) L. May and T. J. J. Müller, Dithieno[1,4]thiazines and Bis[1]benzothieno[1,4]thiazines—Organometallic Synthesis and Functionalization of Electron Density Enriched Congeners of Phenothiazine, *Molecules*, 2020, **25**, 2180; (b) C. Dostert, C. Wanstrath, W. Frank and T. J. J. Müller, 4H-Dithieno[2,3-*b*: 3',2'-*e*][1,4]thiazines – synthesis and electronic properties of a novel class of electron rich redox systems, *Chem. Commun.*, 2012, **48**, 7271–7273; (c) L. May and T. J. J. Müller, Electron-Rich Phenothiazine Congeners and Beyond: Synthesis and Electronic Properties of Isomeric Dithieno[1,4]thiazines, *Chem. – Eur. J.*, 2020, **26**, 12111–12118.
  - 7 The byproduct dibenzo[*d,d'*]thieno[3,2*b'*;4,5-*b'*]dithiophene is assigned by its <sup>1</sup>H and <sup>13</sup>C NMR spectra and its mass spectrum (see ESI, chpt. 1.2.6.1†).
  - 8 M. Mantina, A. C. Chamberlin, R. Valero, C. J. Cramer and D. G. Truhlar, Consistent van der Waals Radii for the Whole Main Group, *J. Phys. Chem. A*, 2009, **113**, 5806–5812.
  - 9 P. R. Spackman, M. J. Turner, J. J. McKinnon, S. K. Wolff, D. J. Grimwood, D. Jayatilaka and M. A. Spackman, *CrystalExplorer*: a program for Hirshfeld surface analysis, visualization and quantitative analysis of molecular crystals, *J. Appl. Crystallogr.*, 2021, **54**, 1006–1011.
  - 10 V. Coropceanu, J. Cornil, D. A. da Silva Filho, Y. Olivier, R. Silbey and J.-L. Brédas, Charge Transport in Organic Semiconductors, *Chem. Rev.*, 2007, **107**, 926–952.
  - 11 K. Takimiya, S. Shinamura, I. Osaka and E. Miyazaki, Thienoacene-Based Organic Semiconductors, *Adv. Mater.*, 2011, **23**, 4347–4370.
  - 12 (a) Z. Chen, C. S. Wannere, C. Corminboeuf, R. Puchta and P. v. R. Schleyer, Nucleus-Independent Chemical Shifts (NICS) as an Aromaticity Criterion, *Chem. Rev.*, 2005, **105**, 3842–3888; (b) A. Stanger, Nucleus-Independent Chemical Shifts (NICS): Distance Dependence and Revised Criteria for Aromaticity and Antiaromaticity, *J. Org. Chem.*, 2006, **71**, 883–893.
  - 13 (a) M. J. Frisch, G. W. Trucks, H. B. Schlegel, G. E. Scuseria, M. A. Robb, J. R. Cheeseman, G. Scalmani, V. Barone, B. Mennucci, G. A. Petersson, H. Nakatsuji, M. Caricato, X. Li, H. P. Hratchian, A. F. Izmaylov, J. Bloino, G. Zheng, J. L. Sonnenberg, M. Hada, M. Ehara, K. Toyota, R. Fukuda, J. Hasegawa, M. Ishida, T. Nakajima, Y. Honda, O. Kitao, H. Nakai, T. Vreven, J. J. A. Montgomery, J. E. Peralta, F. Ogliaro, M. Bearpark, J. J. Heyd, E. Brothers, K. N. Kudin, V. N. Staroverov, R. Kobayashi, J. Normand, K. Raghavachari, A. Rendell, J. C. Burant, S. S. Iyengar, J. Tomasi, M. Cossi, N. Rega, J. M. Millam, M. Klene, J. E. Knox, J. B. Cross, V. Bakken, C. Adamo, J. Jaramillo, R. Gomperts, R. E. Stratmann, O. Yazyev, A. J. Austin, R. Cammi, C. Pomelli, J. W. Ochterski, R. L. Martin, K. Morokuma, V. G. Zakrzewski, G. A. Voth, P. Salvador, J. J. Dannenberg, S. Dapprich, A. D. Daniels, O. Farkas, J. B. Foresman, J. V. Ortiz, J. Cioslowski and D. J. Fox, *Gaussian 09, Revision A.02*, Gaussian Inc., Wallingford CT, 2016; (b) E. Runge and E. K. U. Gross, Density-Functional Theory for Time-Dependent Systems, *Phys. Rev. Lett.*, 1984, **52**, 997–1000; (c) R. Bauernschmitt and R. Ahlrichs, Treatment of electronic excitations within the adiabatic approximation of time dependent density functional theory, *Chem. Phys. Lett.*, 1996, **256**, 454–464.
  - 14 (a) K. Deuchert and S. Hünig, Multistage Organic Redox Systems – A General Structural Principle, *Angew. Chem., Int. Ed. Engl.*, 1978, **17**, 875–886; (b) K. Nakasuji, New multistage redox systems and new organic molecular metals, *Pure Appl. Chem.*, 1990, **62**, 477–482; (c) K. Takahashi, Conjugation-extended ring assemblies with central heterocycles – New multistage redox systems, *Pure Appl. Chem.*, 1993, **65**, 127–134.
  - 15 D. T. Clark, J. N. Murrell and J. M. Tedder, The magnitudes and signs of the inductive and mesomeric effects of the halogens, *J. Chem. Soc.*, 1963, 1250–1253.
  - 16 L. C. Allen, Electronegativity is the average one-electron energy of the valence-shell electrons in ground-state free atoms, *J. Am. Chem. Soc.*, 1989, **111**, 9003–9014.
  - 17 (a) A. V. Marenich, C. J. Cramer and D. G. Truhlar, Universal Solvation Model Based on Solute Electron Density and on a Continuum Model of the Solvent Defined by the Bulk Dielectric Constant and Atomic Surface Tensions, *J. Phys. Chem. B*, 2009, **113**, 6378–6396; (b) Y. Fu, L. Liu, H.-Z. Yu, Y.-M. Wang and Q.-X. Guo, Quantum-Chemical Predictions of Absolute Standard Redox Potentials of Diverse Organic Molecules and Free Radicals in Acetonitrile, *J. Am. Chem. Soc.*, 2005, **127**, 7227–7234.
  - 18 S. Stoll and A. Schweiger, EasySpin, a comprehensive software package for spectral simulation and analysis in EPR, *J. Magn. Reson.*, 2006, **178**, 42–55.
  - 19 (a) A. P. W. Schneeweis, A. Neidlinger, G. J. Reiss, W. Frank, K. Heinze and T. J. J. Müller, Radical cation and dication of a 4H-dithieno[2,3-*b*: 3',2'-*e*][1,4]-thiazine, *Org. Chem. Front.*, 2017, **4**, 839–846; (b) F. L. Rupérez, J. C. Conesa and J. Soria, Electron spin resonance study of the influence of the nitrogen substituent on the conformation and spin density distribution of phenothiazine derivatives, *J. Chem. Soc., Perkin Trans. 2*, 1986, 391–395.
  - 20 C. Adamo and V. Barone, Toward Reliable Density Functional Methods without Adjustable Parameters: The PBE0 Model, *J. Chem. Phys.*, 1999, **110**, 6158–6170.

